Patrick E. Hopkins[1]
Engineering Sciences Center,
Sandia National Laboratories,
Albuquerque, NM 87185
e-mail: pehopki@sandia.gov

Bryan Kaehr
Engineering Sciences Center,
Sandia National Laboratories,
Albuquerque, NM 87185;
Department of Chemical and Nuclear Engineering,
University of New Mexico,
Albuquerque, NM 87106

Leslie M. Phinney
Fellow ASME

Timothy P. Koehler

Anne M. Grillet

Engineering Sciences Center,
Sandia National Laboratories,
Albuquerque, NM 87185

Darren Dunphy

Fred Garcia

Department of Chemical and Nuclear Engineering,
University of New Mexico,
Albuquerque, NM 87106

C. Jeffrey Brinker
Engineering Sciences Center,
Sandia National Laboratories,
Albuquerque, NM 87185;
Department of Chemical and Nuclear Engineering,
University of New Mexico,
Albuquerque, NM 87106

Measuring the Thermal Conductivity of Porous, Transparent SiO_2 Films With Time Domain Thermoreflectance

Nanocomposites offer unique capabilities of controlling thermal transport through the manipulation of various structural aspects of the material. However, measurements of the thermal properties of these composites are often difficult, especially porous nanomaterials. Optical measurements of these properties, although ideal due to the noncontact nature, are challenging due to the large surface variability of nanoporous structures. In this work, we use a vector-based thermal algorithm to solve for the temperature change and heat transfer in which a thin film subjected to a modulated heat source is sandwiched between two thermally conductive pathways. We validate our solution with time domain thermoreflectance measurements on glass slides and extend the thermal conductivity measurements to SiO_2-based nanostructured films. [DOI: 10.1115/1.4003548]

Keywords: time domain thermoreflectance, thermal conductivity, differential-effective medium theory, porous SiO_2

1 Introduction

Nanocomposites offer unique capabilities of controlling thermal transport through the manipulation of various structural aspects of the material [1]. Porous micro- and nanocomposite materials have been of recent interest due to the strong boundary scattering effects, causing a controlled reduction in the thermal conductivity [2–7]. This reduction has resulted in amorphous porous nanomaterials exhibiting thermal conductivities lower than the theoretical minimum [6]. With continued reduction in characteristic lengths of materials systems of interest, measurement of these porous composite materials will become more difficult. For example, the 3ω technique [8], which is a contact-based resistive thermometry method of determining the thermal conductivity κ, typically operates at heating event modulation frequencies where the penetration depth of the thermal wave would exceed the thickness of the thin film of interest [9] (the thermal penetration depth of a modulated heat source is given by $\delta \approx \sqrt{2D/\omega}$, where D is the thermal diffusivity, defined as $D=\kappa/C$, where C is the heat capacity, and ω is the angular frequency of the modulated heating event defined as $\omega=2\pi f$, where f is the modulation frequency). This can cause interference from underlying substrate materials [10], and various correction factors must be employed to account for thermal confinement and spreading in the film [11]. Optical, noncontact meth-

[1]Corresponding author.

Contributed by the Heat Transfer Division of ASME for publication in the JOURNAL OF HEAT TRANSFER. Manuscript received June 7, 2010; final manuscript received January 25, 2011; published online March 9, 2011. Assoc. Editor: Kenneth Goodson.

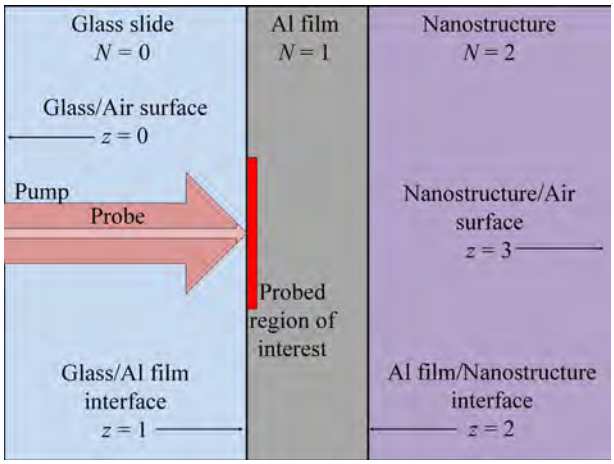

Fig. 1 Geometry of samples interrogated in this work. A sample is adjacent onto a thin Al film that is evaporated on a glass slide. TDTR is performed on the Al film by probing through the glass slide. Bidirectional heat transfer must be accounted for in this case since many samples that can be measured in this configuration have thermal diffusivities less than glass.

ods, such as short pulsed, pump-probe thermoreflectance ((or time domain thermoreflectance (TDTR)) [12,13], have been used to measure κ in a wide array of nanoscale films and composite systems [7,14–23]. Typical operation frequencies of TDTR measurements are in the 1–10 MHz regime, which ensures higher spatial resolution compared with the contact-based resistive thermometry approaches previously discussed. However, the optical nature of these thermoreflectance techniques requires an optically flat, smooth, reflective surface to accurately measure the reflectivity and the subsequent thermal properties, which is difficult to achieve in many porous and amorphous nanocomposites. Recently, Ge et al. [23] and Schmidt et al. [20] used TDTR to measure the thermal conductivity of samples using a slightly different sample geometry than traditionally employed. In these works, the samples of interest were placed on a glass substrate coated with a thin metal film. The pump and probe laser pulses were reflected by the metal transducer through the glass, and the change in the TDTR signal was used to deduce the thermal conductivity of the adjacent liquid. The sample geometry probed by the work of Ge et al. and Schmidt et al. is shown in Fig. 1.

In this work, we solve the heat conduction equation in a multilayer stack of materials with a modulated source at any location in the multilayer stack. This approach, which is based on Feldman's algorithm [24], can account for bidirectional heat transfer to model heat transfer after modulated laser heating in the event that spatial location of the heat event cannot be considered as semi-insulative. In the next section, we derive a solution to the heat equation in the frequency domain accounting for bidirectional heat transfer. We also show the frequency regime where one-dimensional heat transfer will dominate the thermal processes in a multilayer stack. We validate our solution with TDTR measurements on glass slides and extend the thermal conductivity measurements to porous SiO_2-based nanostructured films. We measure the thermal conductivity of two different types of SiO_2 films. One type of film is nanoporous while the other type is comprised of close-packed SiO_2 spherical particles. These two films, along with previous data, allow us to evaluate a well known theory for thermal transport in effective media. We describe the sample fabrication and other experimental considerations in Sec. 3 and discuss the results from our thermal analysis on the SiO_2-based nanostructures in Sec. 4.

2 Thermal Model

The recent work by Schmidt et al. [20] discussed in detail how to apply Carslaw and Jaeger's thermal algorithm for heat transfer in a composite slab [25] to the sample geometry shown in Fig. 1. This algorithm accounts for bidirectional heat transfer through simultaneous solution of two thermal matrices describing the heat transfer from a modulated heat source. However, Feldman's [24] algorithm to solve the heat diffusion equation for a general multilayer stack subjected to a modulated heat source can also be used to solve this geometry. Feldman's algorithm also easily incorporates the thermal boundary conductance h at each material interface [26]. In the remainder of this section, we use Feldman's development to solve for the temperature change in a composite slab in which a modulated source is deposited in a material sandwiched between two other conductive materials. From this, we derive an explicit solution for the temperature change at one side of the sandwiched material. This provides a useful temperature solution for future studies involving modulated thermal sources imparted in buried nanosystems.

The approach in Feldman's treatment is to define vector components of counterpropagating thermal waves in each layer of the multilayer system to solve for the temperature immediately adjacent on either side of the heat source. We consider the nomenclature and geometry shown in Fig. 1, where the interface number z corresponds to the interface to the left of the material layer N. We assume that $N=0$ and 2 are semi-infinite, which is valid for typical time scales and modulation frequencies in TDTR (this will be addressed in more detail later). In the remainder of this section, we will derive the vector-based algorithm to treat modulated heat transfer in the composite slab geometry shown in Fig. 1.

Let us begin by considering a slab of material. The solution to the temperature distribution in material N can be expressed as the sum of exponential terms representing thermal waves traveling in the $+x$ and $-x$ directions given by

$$T(x) = T_N^+ \exp[q_N x] + T_N^- \exp[-q_N x] \tag{1}$$

where T_N^+ and T_N^- are complex constants representing the temperature above ambient. The thermal wave vector q_N is determined from the solution to the heat equation and depends on the dimensionality considered during thermal transport. As discussed by Hopkins et al. [27], the axially symmetric and one-dimensional heat equations can be applied to TDTR experiments depending on the modulation frequency. Therefore, the temperature above ambient can be treated as a two-dimensional vector expressed as

$$\tilde{T} = \begin{bmatrix} T_N^+(x) \\ T_N^-(x) \end{bmatrix} \tag{2}$$

where the vector components correspond to the first and second terms in Eq. (1). Given a material of thickness d and referring to Fig. 1, the temperature at the left end ($x=0$) is related to the temperature at the right end ($x=d$) by

$$\begin{bmatrix} T_N^+(0) \\ T_N^-(0) \end{bmatrix} = \begin{bmatrix} \exp[-q_N d_N] & 0 \\ 0 & \exp[q_N d_N] \end{bmatrix} \begin{bmatrix} T_N^+(d_N) \\ T_N^-(d_N) \end{bmatrix} \tag{3}$$

Again, referring to Fig. 1, the temperature to the left of some interface $z=N+1$ in layer material N is related to the temperature to the right of that interface in material $N+1$ by

$$\begin{bmatrix} T_N^+(d_N) \\ T_N^-(d_N) \end{bmatrix} = \frac{1}{2} \begin{bmatrix} 1 + \frac{\gamma_{N+1}}{\gamma_N} - \frac{\gamma_{N+1}}{h_{z=N+1}} & 1 - \frac{\gamma_{N+1}}{\gamma_N} + \frac{\gamma_{N+1}}{h_{z=N+1}} \\ 1 - \frac{\gamma_{N+1}}{\gamma_N} - \frac{\gamma_{N+1}}{h_{z=N+1}} & 1 + \frac{\gamma_{N+1}}{\gamma_N} + \frac{\gamma_{N+1}}{h_{z=N+1}} \end{bmatrix} \times \begin{bmatrix} T_{N+1}^+(0) \\ T_{N+1}^-(0) \end{bmatrix} \tag{4}$$

where $\gamma_N = \kappa_N q_N$. Equations (3) and (4) give the heat transfer

through a given material and across an interface of two materials. However, boundary conditions must be imposed.

We will now switch to notation specific to the geometry in Fig. 1. As previously mentioned for the thermal transport problem in this work, we assume that layers 0 and 2 are semi-infinite and the modulated heat source is deposited on the surface of the metal film (layer 1). Therefore, we choose

$$\begin{bmatrix} T_0^+(0) \\ T_0^-(0) \end{bmatrix} = T_0(x=0)\begin{bmatrix} 1 \\ 0 \end{bmatrix} \tag{5}$$

and

$$\begin{bmatrix} T_2^+(0) \\ T_2^-(0) \end{bmatrix} = T_2(x=d)\begin{bmatrix} 0 \\ 1 \end{bmatrix} \tag{6}$$

which ensures that $T(\pm\infty)=0$. The temperature just to the left of the heat source is obtained by successively applying Eqs. (3) and (4) to Eq. (5), and this temperature is described by

$$\begin{bmatrix} T_1^+(0^-) \\ T_1^-(0^-) \end{bmatrix} = T_0(x=0)\begin{bmatrix} A^+ \\ A^- \end{bmatrix} \tag{7}$$

where A^+ and A^- are the components of a vector $\tilde{A}$ given by

$$\tilde{A} = \frac{1}{2}\begin{bmatrix} 1+\frac{\gamma_0}{\gamma_1}-\frac{\gamma_0}{h_{z=1}} & 1-\frac{\gamma_0}{\gamma_1}+\frac{\gamma_0}{h_{z=1}} \\ 1-\frac{\gamma_0}{\gamma_1}-\frac{\gamma_0}{h_{z=1}} & 1+\frac{\gamma_0}{\gamma_1}+\frac{\gamma_0}{h_{z=1}} \end{bmatrix}\begin{bmatrix} \exp[q_0 d_0] & 0 \\ 0 & \exp[-q_0 d_0] \end{bmatrix} \times \begin{bmatrix} 1 \\ 0 \end{bmatrix} \tag{8}$$

Similarly, the temperature just to the right of the heat source is obtained by successively applying Eqs. (3) and (4) to Eq. (6), and this temperature is described by

$$\begin{bmatrix} T_1^+(0^+) \\ T_1^-(0^+) \end{bmatrix} = T_2(x=d)\begin{bmatrix} B^+ \\ B^- \end{bmatrix} \tag{9}$$

where B^+ and B^- are the components of a vector $\tilde{B}$ given by

$$\tilde{B} = \frac{1}{2}\begin{bmatrix} \exp[-q_1 d_1] & 0 \\ 0 & \exp[q_1 d_1] \end{bmatrix}\begin{bmatrix} 1+\frac{\gamma_2}{\gamma_1}-\frac{\gamma_2}{h_{z=2}} & 1-\frac{\gamma_2}{\gamma_1}+\frac{\gamma_2}{h_{z=2}} \\ 1-\frac{\gamma_2}{\gamma_1}-\frac{\gamma_2}{h_{z=2}} & 1+\frac{\gamma_2}{\gamma_1}+\frac{\gamma_2}{h_{z=2}} \end{bmatrix} \times \begin{bmatrix} \exp[-q_2 d_2] & 0 \\ 0 & \exp[q_2 d_2] \end{bmatrix}\begin{bmatrix} 1 \\ 0 \end{bmatrix} \tag{10}$$

From Feldman's solution [24], we know that

$$T_0(x=0) = \frac{1}{2\gamma_1}\frac{B^+ + B^-}{A^+B^- - A^-B^+} \tag{11}$$

and

$$T_2(x=d) = \frac{1}{2\gamma_1}\frac{A^+ + A^-}{A^+B^- - A^-B^+} \tag{12}$$

Note that if dealing with an insulated metal film surface, such as in a more traditional TDTR sample configuration, $A^+=A^-=1/2$, and Eq. (11) gives the temperature change on the surface of the metal film [13]. However, in the case considered in Fig. 1, we are interested in $T_1(x=0)$, which can be determined with Eq. (1) and either by using Eq. (11) in Eq. (7) or Eq. (12) in Eq. (9). For example, plugging Eq. (11) into Eq. (7) gives

$$\begin{bmatrix} T_1^+(0^-) \\ T_1^-(0^-) \end{bmatrix} = \frac{1}{2\gamma_1}\frac{B^+ + B^-}{A^+B^- - A^-B^+}\begin{bmatrix} A^+ \\ A^- \end{bmatrix} \tag{13}$$

and with Eq. (1), we obtain the temperature at the surface of the metal film given by

$$T_1(x=0) = T_1^+(0^-) + T_1^-(0^-) \tag{14}$$

Similarly, as a check, we can perform the operation using Eq. (12) with Eq. (9), yielding

$$\begin{bmatrix} T_1^+(0^+) \\ T_1^-(0^+) \end{bmatrix} = \frac{1}{2\gamma_1}\frac{A^+ + A^-}{A^+B^- - A^-B^+}\begin{bmatrix} B^+ \\ B^- \end{bmatrix} \tag{15}$$

which leads to

$$T_1(x=0) = T_1^+(0^+) + T_1^-(0^+) \tag{16}$$

This makes sense as this implies that $T_1^+(0^+)=T_1^+(0^-)$ and $T_1^-(0^+)=T_1^-(0^-)$, which is necessary for continuity.

To calculate the temperature rise on the surface of the metal film, the thermal wave vector in each layer q_N must be determined. As previously discussed, q_N is determined from the solution to the heat equation and depends on the dimensionality considered during thermal transport. Assuming isotropic media in the individual layers, the thermal wave vectors are given by [27]

$$q_{N,\mathrm{Ax}}^2 = k^2 + \frac{iC_N\omega}{\kappa_N} \tag{17}$$

for the axially symmetric model, where k is the Hankel transform variable. As previously mentioned, ω is the angular frequency of the modulated heating event defined as $\omega=2\pi f$, where f is the modulation frequency. For the one-dimensional model,

$$q_{N,\mathrm{1D}}^2 = \frac{iC_N\omega}{\kappa_N} \tag{18}$$

The temperature rise at the surface of the confined metal film detected by a probe pulse of radius w_{pr} due to the excitation of a pump pulse with absorbed power a and radius w_{pm} is calculated by convoluting Eq. (14) (or Eq. (16)) with the pump beam distribution then averaging over the probe beam distribution. This leads to the predicted temperature rise in the frequency domain during pump-probe experiments using the axially symmetric model of [13,22]

$$\theta_{\mathrm{Ax}} = \frac{a}{2\pi w_{\mathrm{pm}}^2}\int_0^\infty T_1(x=0)\exp\left[\frac{-k^2(w_{\mathrm{pr}}^2+w_{\mathrm{pm}}^2)}{8}\right]kdk \tag{19}$$

and that of the one-dimensional model of [27]

$$\theta_{\mathrm{1D}} = \frac{aw_{\mathrm{pr}}^2}{\pi w_{\mathrm{pm}}^4}T_1(x=0) \tag{20}$$

Figure 2 shows the ratio of the absolute value of the real to imaginary solution of Eq. (19), $\mathrm{rri}_{\mathrm{Ax}}$ ($\mathrm{rri}_{\mathrm{Ax}}=\mathrm{abs}[\mathrm{Re}[\theta_{\mathrm{Ax}}]/\mathrm{Im}[\theta_{\mathrm{Ax}}]]$), as a function of modulation frequency for five different values for the thermal diffusivity of layer 2, $D=10^{-7}$ m^2 s^{-1}, 10^{-6} m^2 s^{-1}, 10^{-5} m^2 s^{-1}, 10^{-4} m^2 s^{-1}, and 10^{-3} m^2 s^{-1}. Assuming a heat capacity of 1 MJ m^{-3} K^{-1}, this corresponds to a range of thermal conductivities of layer 2 of 0.1–1000 W m^{-1} K^{-1}. We assume a sample geometry shown in Fig. 1 with a 100 nm thick Al film. For these calculations, h_1 (the thermal boundary conductance between the Al and the glass) is taken as 50 MW m^{-2} K^{-1}, κ_0 (the thermal conductivity of the glass) is taken as 1.4 W m^{-1} K^{-1}, κ_1 (the thermal conductivity of the Al film) is taken as 237 W m^{-1} K^{-1}, and h_2 (the thermal boundary conductance between the Al film and layer 2) is assumed as 50 MW m^{-2} K^{-1} [20]. In reality, and as will be quantified later, the thermal conductivity of the Al film will be slightly reduced from the bulk value (we determine a thermal conductivity of an ~90 nm film as 200 W m^{-1} K^{-1}); however, the TDTR signal is nearly entirely insensitive to the thermal conductivity of the Al film over the pump-probe delay time used to determine κ of adjacent materials. We assume a heat capacity of glass as 1.9 MJ m^{-3} K^{-1} and that of the Al film as 2.44 MJ m^{-3} K^{-1} [28], which we will assume for the remainder of this work. In the limit of an extremely high diffusivity of layer 2, the frequency domain solution relaxes to that predicted, assum-

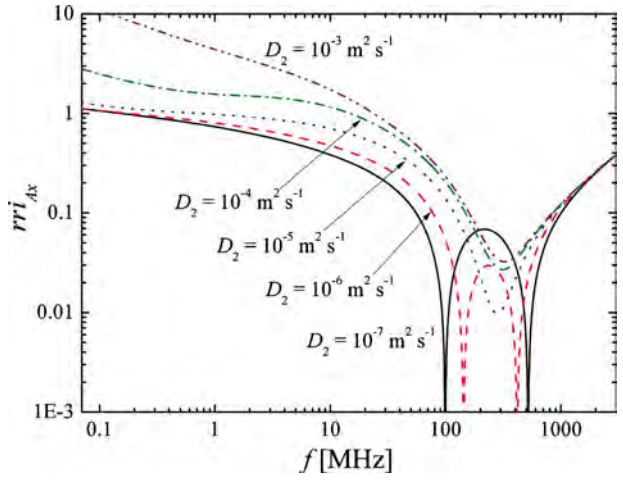

Fig. 2 Frequency domain solution to the axially symmetric heat equation for the sample geometry shown in Fig. 1 as a function of modulation frequency for five different values for the thermal diffusivity of layer 2, $D=10^{-7}$ m^2 s^{-1}, 10^{-6} m^2 s^{-1}, 10^{-5} m^2 s^{-1}, 10^{-4} m^2 s^{-1}, and 10^{-3} m^2 s^{-1}. As discussed in the text, bulk thermophysical properties are assumed for the Al film (layer 1) and the glass slide (layer 0). Both the glass and the nanostructure (layer 2) are assumed to be semi-infinite. The value plotted in this figure is the absolute value of the ratio of the real to imaginary solution of Eq. (19).

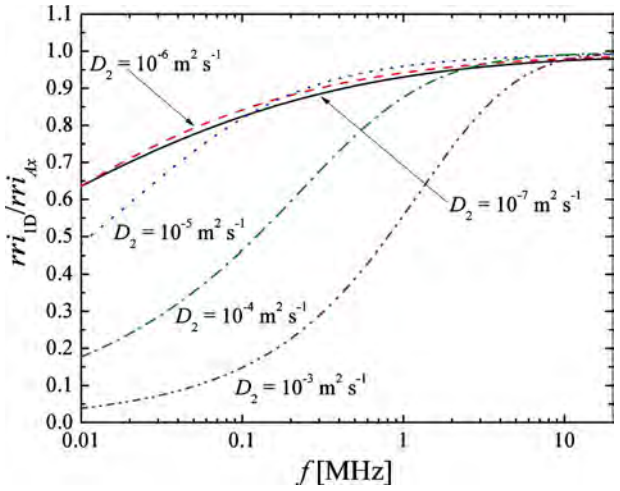

Fig. 3 Ratio of rri_{1D} to rri_{Ax} for the range of modulation frequencies typical in TDTR experiments assuming that $w_{pr}=w_{pm}=17$ μm. When $rri_{1D}/rri_{Ax}=1$, the heat transfer is purely one dimensional. For frequencies above 5 MHz, we find that the value of rri_{1D}/rri_{Ax} approaches 1, allowing us to safely approximate the heat transport as one dimensional for our sample geometry studied in this work (depicted in Fig. 1).

ing an insulated surface (i.e., layer 0 has properties of air). In this case, the thermal wave produced from the modulated heating does not see the glass on the front surface since the diffusivity of layer 2 is so much higher than that of the glass. As the diffusivity of layer 2 approaches that of the glass, the solutions converge at low frequencies.

3 Experimental Considerations

We fabricated two different types of silica-based porous films on Al films evaporated onto glass substrates to form the sample geometry similar to that shown in Fig. 1. The thicknesses of the Al films were verified with picosecond ultrasonics [29,30]. The first type of films were made from colloidal silica particles that were convectively deposited (CD) to form a microporous layer of silica of approximately 1 μm thick. These CD films were deposited on 100 nm Al film evaporated on Corning 2947 microscope slides. Convective deposition is an evaporation-driven process in which a thin film of a particle-laden solvent is dried in a controlled manner, resulting in a colloidal structure on the substrate. As the thin film evaporates, convection is induced in the bulk, and particles are drawn toward the growing colloidal structure. By varying the parameters governing the evaporation of the thin solvent film (i.e., particle concentration, solvent volatility, substrate wettability, etc.), various types of colloidal crystals can be formed [31]. In the CD film deposition, 30 ml of a 10% (by volume) particle concentration in ethanol was placed between the Al film and a second glass slide held at an angle of approximately 26 deg. The angled slide was translated relative to the stationary horizontal slide, creating a thin film of the solvent. A close-packed, single layer structure of 1 μm silica microspheres (Fuso SP-1B) was formed by moving the angled slide at $v=10$ μm/s relative to the stationary substrate. We refer to these films as the CD silica films.

The other types of silica nanostructured films were fabricated by evaporation-induced self-assembly (EISA). These EISA films were fabricated on an 85 nm Al film deposited on VWR microcover glass (No. 48368040). Through the use of a monoacyl glyceride, glycerol monooloeate (GMO), this EISA approach can template well-defined pore networks in silica films. In EISA, a homogeneous alcohol/water solution of a soluble silica precursor, acid catalyst, and GMO template (present at a concentration much less than where bulk mesophases appear) undergoes preferential evaporation of alcohol during film coating, thus increasing the concentration of the template and driving the self-assembly of nanostructured GMO mesophases where water is replaced by nonvolatile silica. The GMO template can then be removed by either acid extraction or UV/O_3 treatment, leaving a porous silica "fossil" of the original mesophase. Interestingly, we find that the pore size distribution of the resulting porous film is dependent on which of these removal techniques is used; acid extraction yields an average pore size of about 10 nm, while UV/O_3 treatment gives an average pore size of 4 nm estimated from transmission electron microscopy (TEM) images. The total film porosity is $\sim$30% measured via spectroscopic ellipsometry and independent of pore size and structure. We test four different types of EISA silica films; we refer to these films as the EISA silica films.

The thermal conductivities of the silica-based nanostructured films were measured with TDTR [12,13,32]. Details of our specific TDTR experimental setup are discussed elsewhere [27]. In short, an 80 MHz, 90 fs pulse train is split into a pump path and a probe path. The pump path is further modulated with an electro-optic modulator (EOM) and the probe path is temporally delayed with respect to the pump path via a mechanical delay stage. The pump and probe are focused down to the Al film through the glass substrate to $1/e^2$ radii of $\sim$17 μm. The reflectance of the probe pulses is collected with a silicon photodiode, and the thermoreflectance signal is monitored with a lock-in amplifier triggered at the EOM frequency.

Varying the pump modulation frequency can cause the TDTR signal to increase in sensitivity to various aspects of thermal transport [21,22,27,33]. In this work, we are interested in the thermal conductivity of the nanostructured silica films and therefore want to reduce the effects of radial spreading in the Al film while maximizing the sensitivity of the TDTR signal to cross plane transport. To determine the range of modulation frequencies that will cause the TDTR signal to be dominated by cross plane transport, we compare Eq. (19) to Eq. (20) [27]. Figure 3 shows the ratio of rri_{1D} to rri_{Ax} ($rri_{1D}=\text{abs}[\text{Re}[\theta_{1D}]/\text{Im}[\theta_{1D}]]$) for the range of modulation frequencies typical in TDTR experiments. The calculations in Fig. 3 assume that $w_{pr}=w_{pm}=17$ μm to simulate the experimental conditions. When $rri_{1D}/rri_{Ax}=1$, the heat transfer is purely one dimensional. For the sample geometry shown in Fig. 1

for frequencies above 5 MHz, we find that the value of this ratio approaches 1, allowing us to safely approximate the heat transport as one dimensional. For the experiments in this work, we choose a pump modulation frequency of 11 MHz so our signals are not affected by radial heating. An interesting aspect of dimensionality in transport is observed in the lowest diffusivity calculations in Fig. 3 ($D_2 \sim 10^{-6}$ m^2 s^{-1} and 10^{-7} m^2 s^{-1}). As the diffusivity of layer 2 decreases from that comparable to diamond, the trends in the comparative ratio follow similar patterns; lower diffusivities mean that one-dimensional transport can be assumed, and the curvature as a function of frequency follows similar trends. However, in the lowest diffusivity layers, the curvature as a function of frequency does not resemble that of the other diffusivity curves. This is due to the fact that as the frequency increases, the thermal penetration depth becomes smaller such that the density of heat deposited in the Al film is larger. When the Al film is sandwiched between two relatively nonconducting layers, radial diffusion in the conducting Al film spreads heat much more quickly than in the layers so that the effect of radial spreading in the Al film affects the dimensionality of the heat flow in the samples as more heat is deposited in the Al film (i.e., as the thermal penetration depth decreases) [27].

Where the thermal models discussed in the previous section predict the temperature change in the frequency domain, TDTR data are related to the change in temperature as a function of time. The output of the lock-in amplifier serves to relate the frequency domain model to the time domain. Details of the lock-in analysis and the relation among temperature change, frequency, pump-probe delay time, and lock-in output are described in detail elsewhere [13,20,22,27]. For TDTR analyses, we look at the ratio of the real to imaginary lock-in outputs $-X/Y$, where X and Y are the real and imaginary components to the output of the lock-in amplifier, which eliminates the need to precisely know the thermoreflectance coefficient of the metal film and gain of the electronic circuit in addition to reducing error due to probe beam drift and dephasing [13]. Note that when analyzing the heat transfer using $-X/Y$, the thermal model need not be normalized to the experimental data since values typically warranting normalization (i.e., thermoreflectance coefficient and electronic gain) cancel out in the division of X and Y. This gives additional sensitivity to more thermophysical properties as compared with analyses in which thermal models are normalized to TDTR data (i.e., when analyzing the heat transfer with the lock-in magnitude ($\sqrt{X^2+Y^2}$) or the real component (X) only). We take four to six TDTR data scans on each sample to ensure reproducibility.

4 Results

In order to accurately determine the thermal conductivity of the silica structures (CD and EISA), we must first determine the thermal boundary conductance at the Al/glass interface and thermal conductivity of the glass. The importance of determining these thermal properties is illustrated by examining the thermal sensitivity over the pump-probe delay time defined as [16,34]

$$S_p = \frac{\partial \ln\left[-\dfrac{X(t)}{Y(t)}\right]}{\partial \ln[p]} \tag{21}$$

where p is some thermophysical property and t is the pump-probe delay time. In this approach, central values of all the necessary thermophysical parameters are prescribed, and one particular property p is slightly perturbed while all other properties are kept constant. In our calculations, we perturb the thermophysical properties by 1%. In this case, we are interested in determining the thermal sensitivity to the thermal conductivity of the glass substrate ($p=\kappa_0$), the thermal boundary conductance between the glass substrate and the Al film ($p=h_1$), the thermal boundary conductance between the Al film and some SiO_2 film ($p=h_2$), and the thermal conductivity of some SiO_2 film ($p=\kappa_2$). For these calculations, we assume a pump modulation frequency of 11 MHz, $h_2=50$ MW m^{-2} K^{-1}, and assume bulk values as our central values for all other thermophysical properties of the glass slide (assumed as bulk SiO_2) and the Al film [28]. We examine three different cases for the thermal properties of the SiO_2 film on side 2: (a) same properties as the glass slide, (b) same heat capacity as the glass slide with half of the thermal conductivity, and (c) thermal properties of air ($C_2=1000$ J m^{-3} K^{-1} and $\kappa_2=0.0257$ W m^{-1} K^{-1}). The thermal sensitivities to κ_0, h_1, h_2, and κ_2 for the three different cases are shown in Fig. 4. The thermal sensitivity to κ_2 and h_2 decreases and the thermal sensitivity to the glass slide thermal properties (κ_0 and h_1) increases as the thermal conductivity of material on side 2 decreases. This is intuitive as heat will more rapidly propagate into the glass as the thermal effusivity of the SiO_2 film decreases. Also, for these cases, there is a relatively low sensitivity to h_2 since the conductance associated with the SiO_2 film on side 2 is much lower than the Al/SiO_2 film interface conductance [35]. In the limit that there is no SiO_2 film and the Al film is adjacent to air on side 2, then the thermal

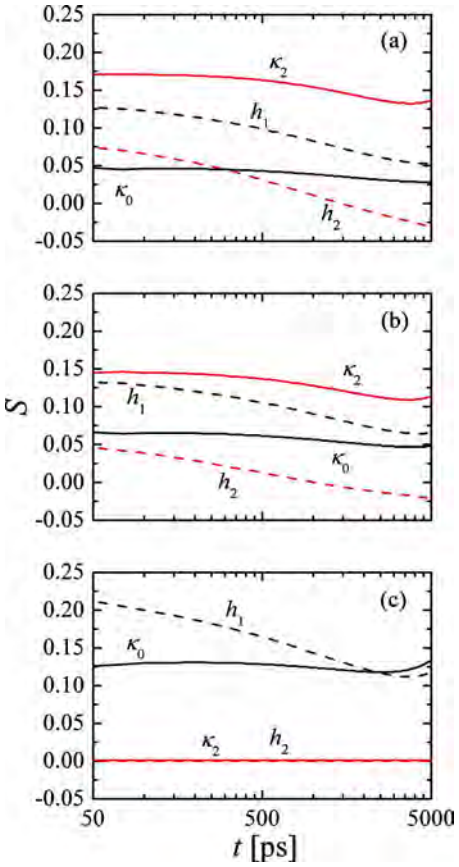

Fig. 4 Thermal sensitivity defined in Eq. (21) to the thermal conductivity of the glass substrate ($p=\kappa_0$), the thermal boundary conductance between the glass substrate and the Al film ($p=h_1$), the thermal boundary conductance between the Al film and some SiO_2 film ($p=h_2$), and the thermal conductivity of some SiO_2 film ($p=\kappa_2$) as a function of time for the measurement geometry shown in Fig. 1. We consider three different cases for the thermal properties of the film on side 2: (a) same properties as the glass slide, (b) same heat capacity as the glass slide with half of the thermal conductivity, and (c) thermal properties of air ($C_2=1000$ J m^{-3} K^{-1} and $\kappa_2=0.0257$ W m^{-1} K^{-1}). Note also that the sensitivity to h_1 is nearly as large as that of κ_2 for cases (a) and (b), elucidating the importance of determining the thermal boundary conductance between the Al film and the glass slide. We assume bulk thermophysical properties for all other thermophysical parameters [28].

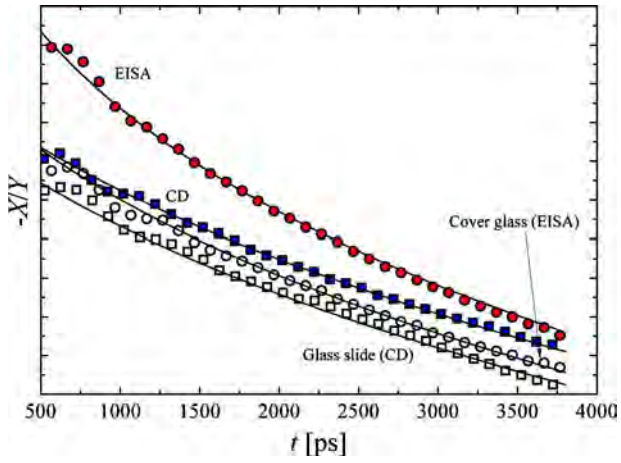

Fig. 5 Representative TDTR data from the samples in this work along with their corresponding best fit thermal models. We probe the Al/cover glass and Al/glass slide samples that have not been coated with EISA or CD silica films from the front (not shown) and back to determine the thermal conductivity of the glass substrate and thermal boundary conductance at the Al/glass interface and verify our thermal model and fitting algorithm.

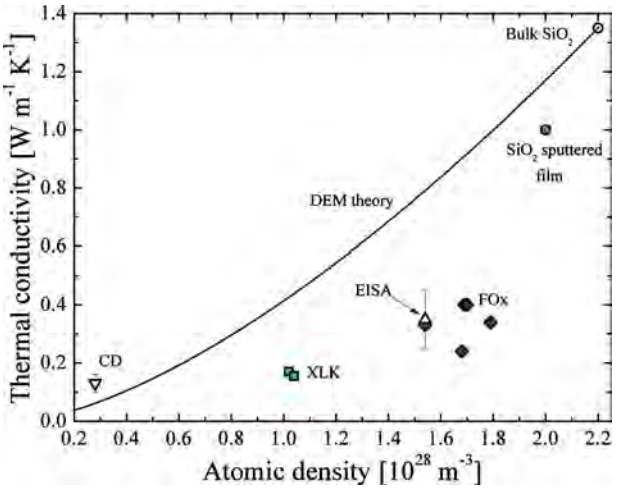

Fig. 6 Average thermal conductivity of the CD and EISA samples compared with previous measurements of the thermal conductivity of SiO_2-based films (SiO_2 sputtered thin film (sputtered), flowable oxide (FO_x), and XLK) and bulk amorphous SiO_2. The EISA and CD thermal conductivities, along with the previous measurements, all show a substantial reduction in thermal conductivity from bulk, and even thin film sputtered SiO_2. The solid line represents the thermal conductivity prediction from the DEM theory.

sensitivity to the air properties goes to zero and that to κ_0 and h_1 is maximized for this measurement geometry. Note also that the sensitivity to h_1 is nearly as large as that of κ_2 for cases (a) and (b), elucidating the importance of determining the thermal boundary conductance between the Al film and the glass slide. Note that the sensitivity of h_1 will decrease as the thermal conductivity of κ_0 decreases as compared with κ_2 so that in the limit where κ_2 approaches that of air (much smaller than κ_2 in a given sample of interest), the sensitivity reduces to that of a more traditional TDTR measurement geometry.

During each Al evaporation run, we included an extra substrate that would not be used for silica film deposition and therefore be used for calibration in determining h_1 and κ_0. We deduce the thermal conductivity of the Al film from electrical conductivity measurements and the Weidemann–Franz law [36]; the thermal conductivity we determine—200 $W\,m^{-1}\,K^{-1}$—is slightly reduced from that of bulk—237 $W\,m^{-1}\,K^{-1}$ (Ref. [28])—although in practice the TDTR signal is relatively insensitive to the thermal conductivity of the Al film over the pump-probe delay time used to determine κ of adjacent materials. Figure 5 shows the TDTR data on the Al/cover glass and Al/glass slide. We probed both on the Al side (more traditional TDTR geometry by probing from the "front") and through the glass (probing from the "back") on the calibration samples. In the back probed sample (and for all the samples in which the TDTR measurements were taken through the glass shown in Fig. 5), slow oscillations occur throughout the first nanosecond; these oscillations are associated with Brillouin backscattering and are similar to those observed by Schmidt et al. [20] in TDTR measurements using the same probing geometry. Probing from the front, we determine an average h and κ with standard deviation among the determined values of the cover glass as 80 ± 10 $MW\,m^{-2}\,K^{-1}$ and 1.25 ± 0.08 $W\,m^{-1}\,K^{-1}$, respectively. Our algorithm when probing from the back yields average best fits of 50 ± 20 $MW\,m^{-2}\,K^{-1}$ and 1.2 ± 0.11 $W\,m^{-1}\,K^{-1}$ in good agreement with the front data. For our thermal model on the EISA samples (which were deposited on the cover glass), we use the values determined from the front side probe, but the agreement with the glass side probe approach verifies our thermal model presented in Sec. 2. We perform the same analysis with the glass slides and determine a best fit h at the Al/glass slide interface and κ of the glass slide as 60 ± 10 $MW\,m^{-2}\,K^{-1}$ and 1.3 ± 0.08 $W\,m^{-1}\,K^{-1}$. In terms of the sample geometry shown in Fig. 1, these values represent κ_0 and h_1 in our thermal model, as previously mentioned.

Representative TDTR data on the CD and EISA films along with the TDTR data from the calibration samples (probing through the cover glass (EISA) and glass slide (CD)) are shown in Fig. 5 along with the best fit model. The average best fit κ and standard deviations on the CD and EISA films are 0.13 ± 0.03 $W\,m^{-1}\,K^{-1}$ and 0.35 ± 0.1 $W\,m^{-1}\,K^{-1}$, respectively. To minimize the fitting error, we adjust h_1 as this property can change based on interface structure and therefore probe location; the values we determine for h_1 are within 18% of those determined from our calibration sample. As previously mentioned, there is a relatively low sensitivity to h_2 since the conductance associated with the SiO_2 film on side 2 is much lower than the Al/SiO_2 film interface conductance [35]. Note in Fig. 5 that the thermoreflectance scans on the cover glass and glass slide with no porous SiO_2 samples (i.e., the adiabatic case or the "air" case in Fig. 4) are different. Although the conductivities of the cover glass and glass slide were measured as slightly different in our calibration, this minute difference in κ_0 is not the cause of this observed change in the thermoreflectance. The main difference between these scans arises due to the differing Al film thicknesses used in the CD and EISA samples as a thicker Al film gives a lower thermoreflectance response $(-X/Y)$ in the temporal domain of interest. We find that the thermal conductivity of the EISA films is independent of the removal technique within the standard deviation among the measured values. The thermal conductivity of these porous silica films is in good agreement with that of SiO_2-based nanoporous films measured with the 3ω technique [6].

Figure 6 compares the thermal conductivity measured in this work (EISA and CD) to the previous measurements of silica-based films—SiO_2 sputtered thin film (sputtered), flowable oxide (FO_x), and extra low-k (XLK) [6]—as a function of sample atomic density. The atomic density n of bulk SiO_2 is 2.2×10^{28} atoms m^{-3}. We determine the EISA density as 70% of bulk SiO_2 calculated from the porosity measurement discussed previously. We estimate the CD sample density as 2.8×10^{27} atoms m^{-3} by comparing the TDTR signal magnitude to

that of bulk SiO_2 [37]; this approach is valid since the silica particles comprising the CD film are upward of 1 μm and the reduction in atomic density in these films is due to the packing density of the particles. We also include data for bulk amorphous SiO_2 [38]. The EISA and CD thermal conductivities, along with the previous measurements, all show a substantial reduction in thermal conductivity from bulk and even thin film sputtered SiO_2. The reduction in conductivity as a function of atomic density for the SiO_2 film is compared with the differential-effective-medium (DEM) theory [39], which predicts that the reduced thermal conductivity is given by

$$\kappa = \kappa_{\text{solid}} \left(\frac{n}{n_{\text{solid}}} \right)^{3/2} \tag{22}$$

where the subscript "solid" refers to the corresponding property of bulk SiO_2. The predictions from Eq. (22) agree well with the CD samples measured in this work, yet overpredict the previously measured SiO_2-based films and the EISA film. This could arise due to the geometry of the pores in previously measured SiO_2-based films and the EISA film, as the DEM theory assumes an infinitesimal volume of spherical voids. However, the CD film is comprised of close-packed silica spheres, which could have a geometry more in line with the original assumptions of the DEM theory.

5 Conclusions

In this work, we solve the heat conduction equation in a multilayer stack of materials with a modulated source at any location in the multilayer stack based on the Feldman algorithm. This approach accounts for bidirectional heat transfer and accurately predicts the thermal processes in TDTR in the "probe from the back" geometry. We theoretically studied the dimensionality of the thermal transport in the frequency domain to determine modulation frequencies and thermal diffusivities where cross plane transport will dominate the heat transfer in a multilayer stack. We then applied our solution to TDTR data to determine the thermal conductivity of SiO_2-based films. One of the film types is nanoporous (EISA) while the other type is comprised of close-packed spherical particles (CD). We compare the measured thermal conductivity to that of nanostructured silica films from the literature and to the DEM theory. The predictions from the DEM theory agree well with the CD samples measured in this work, yet overpredict the previously measured SiO_2-based films and the EISA films. This could arise since the CD film is comprised of close-packed silica spheres, which could have a geometry more in line with the original assumptions of the DEM theory.

Acknowledgment

P.E.H. and B.K. are greatly appreciative for funding from the LDRD Program Office through the Harry S. Truman Fellowship Program. This work was performed, in part, at the Center for Integrated Nanotechnologies, a U.S. Department of Energy, Office of Basic Energy Sciences user facility; the authors would like to thank John Sullivan for assistance regarding work at the Center for Integrated Nanotechnologies. Sandia National Laboratories is a multiprogram laboratory operated by Sandia Corporation, a Lockheed-Martin Co., for the U.S. Department of Energy's National Nuclear Security Administration under Contract No. DE-AC04-94AL85000.

Nomenclature

- a = absorbed laser power of the pump beam, W
- C = heat capacity, J m^{-3} K^{-1}
- D = thermal diffusivity, m^2 s^{-1}
- d = thickness, m
- f = frequency, Hz
- h = thermal boundary conductance, W m^{-2} K^{-1}
- k = Hankel transform variable, m^{-1}
- n = atomic density, m^{-3}
- q = thermal wave vector, m^{-1}
- rri = ratio of real to imaginary solution
- S_p = thermal sensitivity to some parameter p
- T = temperature above ambient, K
- t = pump-probe delay time, s
- w = beam waist, m
- X = real component of lock-in response, V
- x = direction of thermal propagation, m
- Y = imaginary component of lock-in response, V

Greek Symbols

- δ = thermal penetration depth, m
- κ = thermal conductivity, W m^{-1} K^{-1}
- θ = temperature rise, K
- τ = time, s
- ω = angular frequency, rad s^{-1}

Subscripts

- 1D = one dimensional
- Ax = axially symmetric
- N = layer
- pr = probe
- pm = pump
- solid = solid matrix
- z = interface

Superscripts

- $+$ = for wave traveling in the $+x$ direction
- $-$ = for wave traveling in the $-x$ direction

References

[1] Cahill, D. G., Ford, W. K., Goodson, K. E., Mahan, G. D., Majumdar, A., Maris, H. J., Merlin, R., and Phillpot, S. R., 2003, "Nanoscale Thermal Transport," J. Appl. Phys., **93**, pp. 793–818.

[2] Benedetto, G., Boarino, L., and Spangnolo, R., 1997, "Evaluation of Thermal Conductivity of Porous Silicon Layers by a Photoacoustic Method," Appl. Phys. A: Mater. Sci. Process., **64**, pp. 155–159.

[3] Bernini, U., Bernini, R., Maddalena, P., Massera, E., and Rucco, P., 2005, "Determination of Thermal Diffusivity of Suspended Porous Silicon Films by Thermal Lens Techniques," Appl. Phys. A: Mater. Sci. Process., **81**, pp. 399–404.

[4] Hopkins, P. E., Rakich, P. T., Olsson, R. H., El-kady, I. F., and Phinney, L. M., 2009, "Origin of Reduction in Phonon Thermal Conductivity of Microporous Solids," Appl. Phys. Lett., **95**, p. 161902.

[5] Song, D., and Chen, G., 2004, "Thermal Conductivity of Periodic Microporous Silicon Films," Appl. Phys. Lett., **84**, pp. 687–689.

[6] Costescu, R. M., Bullen, A. J., Matamis, G., O'Hara, K. E., and Cahill, D. G., 2002, "Thermal Conductivity and Sound Velocities of Hydrogen-Silsequioxane Low-k Dielectrics," Phys. Rev. B, **65**, p. 094205.

[7] Hopkins, P. E., Norris, P. M., Phinney, L. M., Policastro, S. A., and Kelly, R. G., 2008, "Thermal Conductivity in Nanoporous Gold Films During Electron-Phonon Nonequilibrium," J. Nanomater., **2008**, p. 418050.

[8] Cahill, D. G., 1990, "Thermal Conductivity Measurement From 30 to 750 K: The 3ω Method," Rev. Sci. Instrum., **61**, pp. 802–808.

[9] Koh, Y. K., Singer, S. L., Kim, W., Zide, J. M. O., Lu, H., Cahill, D. G., Majumdar, A., and Gossard, A. C., 2009, "Comparison of the 3ω Method and Time-Domain Thermoreflectance for Measurements of the Cross-Plane Thermal Conductivity of Epitaxial Semiconductors," J. Appl. Phys., **105**, p. 054303.

[10] Olson, B. W., Graham, S., and Chen, K., 2005, "A Practical Extension of the 3ω Method to Multilayer Structures," Rev. Sci. Instrum., **76**, p. 053901.

[11] Borca-Tasciuc, T., Kumar, A. R., and Chen, G., 2001, "Data Reduction in 3ω Method for Thin-Film Thermal Conductivity Determination," Rev. Sci. Instrum., **72**, pp. 2139–2147.

[12] Norris, P. M., Caffrey, A. P., Stevens, R. J., Klopf, J. M., Mcleskey, J. T., and Smith, A. N., 2003, "Femtosecond Pump-Probe Nondestructive Examination of Materials," Rev. Sci. Instrum., **74**, pp. 400–406.

[13] Cahill, D. G., 2004, "Analysis of Heat Flow in Layered Structures for Time-Domain Thermoreflectance," Rev. Sci. Instrum., **75**, pp. 5119–5122.

[14] Chiritescu, C., Cahill, D. G., Nguyen, N., Johnson, D., Bodapati, A., Keblinski, P., and Zschack, P., 2007, "Ultralow Thermal Conductivity in Disordered, Layered WSe_2 Crystals," Science, **315**, pp. 351–353.

[15] Costescu, R. M., Cahill, D. G., Fabreguette, F. H., Sechrist, Z. A., and George, S. M., 2004, "Ultra-Low Thermal Conductivity in W/Al_2O_3 Nanolaminates," Science, **303**, pp. 989–990.

[16] Costescu, R. M., Wall, M. A., and Cahill, D. G., 2003, "Thermal Conductance of Epitaxial Interfaces," Phys. Rev. B, **67**, p. 054302.

[17] Hopkins, P. E., Norris, P. M., Stevens, R. J., Beechem, T., and Graham, S., 2008, "Influence of Interfacial Mixing on Thermal Boundary Conductance Across a Chromium/Silicon Interface," ASME J. Heat Transfer, **130**, p. 062402.
[18] Hopkins, P. E., Stevens, R. J., and Norris, P. M., 2008, "Influence of Inelastic Scattering at Metal-Dielectric Interfaces," ASME J. Heat Transfer, **130**, p. 022401.
[19] Norris, P. M., and Hopkins, P. E., 2009, "Examining Interfacial Diffuse Phonon Scattering Through Transient Thermoreflectance Measurements of Thermal Boundary Conductance," ASME J. Heat Transfer, **131**, p. 043207.
[20] Schmidt, A., Chiesa, M., Chen, X., and Chen, G., 2008, "An Optical Pump-Probe Technique for Measuring the Thermal Conductivity of Liquids," Rev. Sci. Instrum., **79**, p. 064902.
[21] Schmidt, A. J., Cheaito, R., and Chiesa, M., 2009, "A Frequency-Domain Thermoreflectance Method for the Characterization of Thermal Properties," Rev. Sci. Instrum., **80**, p. 094901.
[22] Schmidt, A. J., Chen, X., and Chen, G., 2008, "Pulse Accumulation, Radial Heat Conduction, and Anisotropic Thermal Conductivity in Pump-Probe Transient Thermoreflectance," Rev. Sci. Instrum., **79**, p. 114902.
[23] Ge, Z., Cahill, D. G., and Braun, P. V., 2006, "Thermal Conductance of Hydrophilic and Hydrophobic Interfaces," Phys. Rev. Lett., **96**, p. 186101.
[24] Feldman, A., 1999, "Algorithm for Solutions of the Thermal Diffusion Equation in a Stratified Medium With a Modulated Heating Source," High Temp. - High Press., **31**, pp. 293–298.
[25] Carslaw, H. S., and Jaeger, J. C., 1959, *Conduction of Heat in Solids*, 2nd ed., Oxford University Press, New York, Sec. 3.7, pp. 109–112.
[26] Tong, T., and Majumdar, A., 2006, "Reexamining the 3-Omega Technique for Thin Film Characterization," Rev. Sci. Instrum., **77**, p. 104902.
[27] Hopkins, P. E., Serrano, J. R., Phinney, L. M., Kearney, S. P., Grasser, T. W., and Harris, C. T., 2010, "Criteria for Cross-Plane Dominated Thermal Transport in Multilayer Thin Film Systems During Modulated Laser Heating," ASME J. Heat Transfer, **132**, p. 081302.
[28] Incropera, F., and Dewitt, D. P., 1996, *Fundamentals of Heat and Mass Transfer*, Wiley, New York.
[29] Thomsen, C., Grahn, H. T., Maris, H. J., and Tauc, J., 1986, "Surface Generation and Detection of Phonons by Picosecond Light Pulses," Phys. Rev. B, **34**, pp. 4129–4138.
[30] Thomsen, C., Strait, J., Vardeny, Z., Maris, H. J., Tauc, J., and Hauser, J. J., 1984, "Coherent Phonon Generation and Detection by Picosecond Light Pulses," Phys. Rev. Lett., **53**, pp. 989–992.
[31] Prevo, B. G., Kuncicky, D. M., and Velev, O. D., 2007, "Engineered Deposition of Coatings From Nano- to Micro-Particles: A Brief Review of Convective Assembly at High Volume Fraction," Colloids Surf., A, **311**, pp. 2–10.
[32] Paddock, C. A., and Eesley, G. L., 1986, "Transient Thermoreflectance From Thin Metal Films," J. Appl. Phys., **60**, pp. 285–290.
[33] Koh, Y. K., and Cahill, D. G., 2007, "Frequency Dependence of the Thermal Conductivity of Semiconductor Alloys," Phys. Rev. B, **76**, p. 075207.
[34] Gundrum, B. C., Cahill, D. G., and Averback, R. S., 2005, "Thermal Conductance of Metal-Metal Interfaces," Phys. Rev. B, **72**, p. 245426.
[35] Persson, A. I., Koh, Y. K., Cahill, D. G., Samuelson, L., and Linke, H., 2009, "Thermal Conductance of InAs Nanowire Composites," Nano Lett., **9**, pp. 4484–4488.
[36] Franz, R., and Wiedemann, G., 1853, "Ueber die Warme-Leitungsfahigkeit der matalle," Ann. Phys., **165**, pp. 497–531.
[37] Hopkins, P. E., Kaehr, B., Dunphy, D., and Brinker, C. J., 2011, "Estimating Density Reduction and Phonon Localization From Optical Thermal Conductivity Measurements of Porous Silica and Aerogel Thin Films," Proceedings of the ASME/JSME Eighth Thermal Engineering Joint Conference, Honolulu, HI, Paper No. 44137.
[38] Cahill, D. G., and Pohl, R. O., 1987, "Thermal Conductivity of Amorphous Solids Above the Plateau," Phys. Rev. B, **35**, pp. 4067–4073.
[39] Bruggeman, D. A. G., 1935, "Computation of Different Physical Constants of Heterogeneous Substances. I. Dielectric Constants and Conductivenesses of the Mixing Bodies From Isotropic Substances (Berechnung verschiedener physikalischer Konstanten von heterogenen Substanzen. I. Dielektrizitätskonstanten und Leitfähigkeiten der Mischkörper aus isotropen Substanzen)," Ann. Phys., **416**, pp. 636–664.